MAGNETIC FIELD MAPPING OF A LARGE-GRAIN 1.3 GHz SINGLE-CELL CAVITY*

I. P. Parajuli[†], G. Ciovati[1], J. Delayen, A. Gurevich, Old Dominion University, Norfolk, VA, USA
[1]also at Jefferson Lab, Newport News, VA, USA

Abstract

A new magnetic field mapping system for 1.3 GHz single-cell cavities was developed in order to reveal the impact of ambient magnetic field and temperature gradients during cool-down on the flux trapping phenomenon. Measurements were done at 2 K for different cool-down conditions of a large-grain cavity before and after 120 °C bake. The fraction of applied magnetic field trapped in the cavity walls was ~ 50% after slow cool-down and ~ 20% after fast cool-down. The results showed a weak correlation between between trapped flux locations and hot-spots causing the high-field Q-slope. The results also showed an increase of the trapped flux at the quench location, after quenching, and a local redistribution of trapped flux with increasing RF field.

INTRODUCTION

Pinning of magnetic vortices in superconducting radio-frequency (SRF) cavities upon cooling below the critical temperature is a well-known cause of residual RF losses [1]. The quest towards ever increasing quality factor, Q_0, of bulk Nb cavities at 2 K requires achieving residual resistance values of the order of 1 nΩ.

As a result, understanding the flux trapping mechanisms in Nb cavities has become a growing research topic in recent years [2–18]. The ability to measure the magnitude and distribution of trapped vortices in an SRF cavity is particularly challenging due to the size and shape of a typical cavity. We have developed a magnetic field scanning system (MFSS) which allows mapping of the local magnetic field at the surface of 1.3 GHz single-cell cavities in liquid He (LHe) [19]. Initial results were reported in Ref. [20]. In this contribution we report the results of a systematic study of trapped flux in a 1.3 GHz single-cell cavity before and after baking at 120 °C for 48 h. The location of hot-spots on the cavity outer surface caused by excessive RF heating of the inner surface during the high-power RF test at 2 K was also determined by a temperature mapping system.

EXPERIMENTAL RESULTS

Experimental Setup and Test Procedure

The 1.3 GHz single-cell cavity used for this study, labeled PJ1-1, was fabricated from high-purity, large-grain Nb from OTIC, China, and it had the same shape as that of the TESLA/XFEL cavity [21].

The MFSS has two arms, 180° apart, matching the contour of the cavity. One arm has 8 cryogenic Hall probes, measuring the magnetic field component perpendicular to the cavity surface, B_r, whereas the other arm has 8 pairs of anisotropic magnetoresistance (AMR) sensors. The first AMR sensor in a pair measures the B_r-component while the second sensor measures the magnetic field component tangential to the cavity surface, B_t, within ~ 3 mm of the first one. Details of the characteristics of the two type of sensors can be found in Ref. [22]. The sensors are pushed in contact with the cavity outer surface by soft springs. The two arms with the magnetic field sensors are mounted on a large gear, driven by a stepper motor on the top plate of the cryogenic vertical test stand, allowing a full rotation of the arms around the cavity. Further details about the MFSS and the data acquisition system can be found in Ref. [19].

A static temperature mapping system consisting of 576 thermometers based on 100 Ω carbon resistors was also used to measure the local temperature of the outer surface of the cavity, during the high-power RF test in LHe [23]. The test procedure with the thermometry system assembled onto the cavity consists of:

- cooldown below 9.2 K in a fixed axial dc magnetic field, B_a, while applying a temperature gradient along the cavity axis.
- Fill the cryostat with LHe at 4.3 K and measure $Q_0(T)$ at low RF field as well as the resistance of each thermometer during LHe pump-down to 1.6 K.
- Measure Q_0 as a function of the peak surface RF magnetic field, B_p, at 2 K up to the cavity limit and back to B_p ~ 10 mT, acquiring temperature maps.

After a sequence of tests with the T-mapping system, the cavity was disassembled, high-pressure rinsed (HPRed) with ultra-pure water, re-assembled, evacuated, leak checked and hang on the test stand under static vacuum. The MFSS is assembled onto the cavity and the entire setup is inserted into a vertical cryostat. The typical test procedure of the cavity with the MFSS can be summarized as follows:

- reset of the AMR sensors' magnetization by applying a current pulse at room temperature, in low ambient field, B_a ~ 0.5 μT.
- Cooldown to ~ 10 K and measure the offset voltages of the magnetic field sensors.
- Set B_a and the cooldown rate as the cavity is cooled below T_c.
- Fill the cryostat with LHe at 4.3 K, reduce B_a to ~ 0.1 μT and measure $Q_0(T)$ at low RF field during LHe pump-down to 1.6 K.

- Maintain the He bath temperature at 2.0 K and measure the trapped magnetic field on the cavity surface, with no RF field.
- Measure $Q_0(B_p)$ at 2 K up to the cavity limit and back to $B_p \sim 10$ mT, acquiring magnetic field maps at $B_p \sim$ 21 mT, ~ 82 mT and ~ 132 mT.

This measurement sequence was repeated for multiple cool-down conditions and B_a-values. The ambient magnetic field and the temperature gradient were measured using single-axis cryogenic flux-gate magnetometers and Cernox temperature sensors, respectively, attached to the cavity beam tubes.

The average magnetic flux trapped within the cavity walls, $\langle B_0 \rangle$, can be calculated from the scanned data as:

$$\langle B_0 \rangle = \frac{1}{8N} \sum_{i=1}^{8} \sum_{j=1}^{N} B_{0i,j}, \tag{1}$$

where the index i denotes the sensor number, the index j is the step number in the scan and N is the total number of steps. The angular step size for a full map was $4°$, therefore $N = 90$. For AMR sensors $B_0 = \sqrt{B_r^2 + B_t^2}$, whereas $B_0 = B_r$ for Hall probes.

Test Results Before Baking

The final surface preparation of the cavity inner surface prior to the series of baseline tests consisted of buffered chemical polishing (BCP) and HPR. Figure 1 shows the $Q_0(B_p)$ curves measured during tests with the MFSS for different values of B_a and for either "slow cooldown" (SC), resulting in a temperature gradient $dT/dz = 2 - 13$ mK/cm, or "fast cooldown" (FC), resulting in $dT/dz = 220 - 290$ mK/cm. The cavity performance was limited by the high-field Q-slope [24]. The ratio B_p/E_{acc} for this cavity is 4.12 mT/(MV/m), where E_{acc} is the accelerating gradient. Figure 2 shows the $\langle B_0 \rangle$ obtained from B-maps with AMR sensors at different E_{acc}-values after SC with different B_a-values, showing no significant changes with increasing RF field. Similar results were obtained after FC.

Figure 3 shows an example of the difference between a B_0-map measured at 2 K by AMR sensors at $E_{acc} = 32$ MV/m and that without any RF field, after SC with $B_a \sim 11$ µT, indicating a local redistribution of magnetic flux when increasing the RF field.

Figure 4 shows B_0-maps measured by AMR sensors at 2 K with no RF field for different cooldown conditions, showing a higher amount of trapped flux with higher B_a or with SC, when cooling below 9.2 K. Figure 5 shows $\langle B_0 \rangle$ measured with AMR sensors at 2 K with no RF field and the residual resistance, R_{res}, as a function of the ambient magnetic field during cooldown for FC and SC. The residual resistance was obtained from a least-squares fit of $R_s(T) = G/Q_0(T) = Ae^{-U/kT} + R_{res}$, where $G = 269.8$ Ω is the geometry factor, A and U are fit parameters [25]. The slope of the linear fits in Fig. 5(a) corresponds to the fraction of the applied field trapped in the cavity wall, $\eta = (47 \pm 2)$% for SC and $\eta = (17 \pm 1)$% for FC. Interestingly, the linear fits indicate
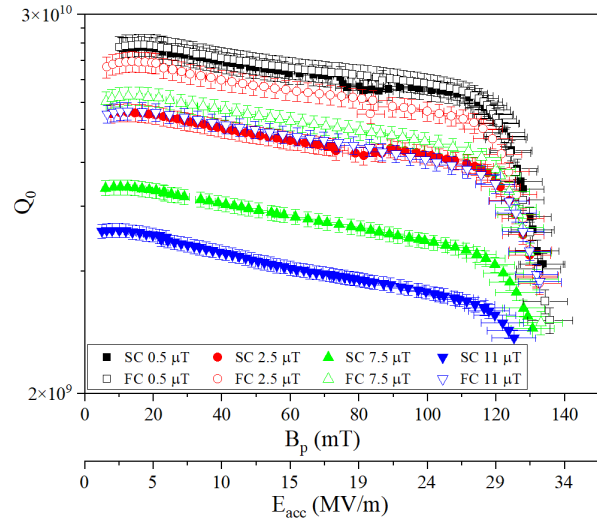

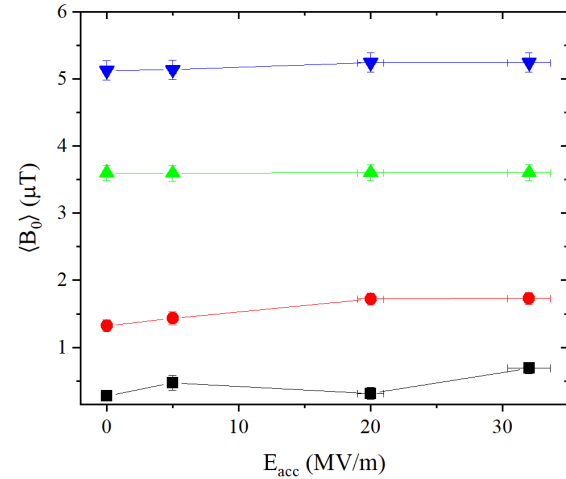Figure 1: $Q_0(B_p)$ measured at 2 K for different ambient magnetic field and cooldown rate at T_c.

Figure 2: $\langle B_0 \rangle$ vs. E_{acc} obtained from B-maps at 2 K with AMR sensors after SC in 0.5 µT (squares), 2.5 µT (circles), 7.5 µT (green triangles), 11 µT (blue triangles). The solid lines are guides to the eyes.

a non-zero intercept. The slope of the linear fits in Fig. 5(b) corresponds to the trapped flux sensitivity, S, multiplied by η. The average trapped flux sensitivity from the two data sets was found to be $S = (5.9 \pm 0.1)$ nΩ/µT.

Figure 6 gives an example of an overlay between the T-map and the B-map, both measured at 2 K and $E_{acc} = 32$ MV/m after FC with $B_a \sim 0.5$ µT. ΔT is the difference between the sensors' temperature and that of the LHe bath. The hot-spots in the T-map result in the high-field Q-slope and no strong correlation was found with regions of trapped flux. A similar conclusion could be made from test results with other cooldown conditions.

Test Results After Baking

Figure 7 shows the $Q_0(B_p)$ curves measured during tests with the MFSS for different values of B_a and for either SC or
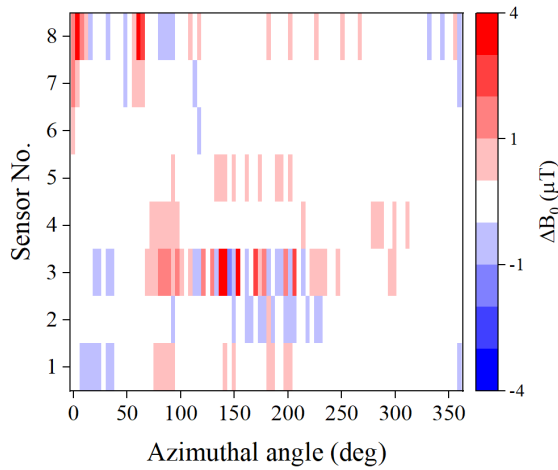
Figure 3: Difference between the B_0-map measured by AMR sensors at E_{acc} = 32 MV/m minus that with no RF field, after SC with $B_a \sim 11\,\mu T$. Sensors 4 and 5 are just below and above the equator weld, respectively.
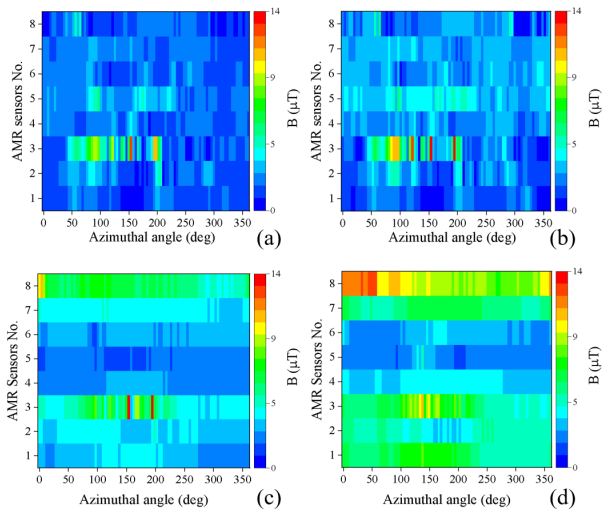

Figure 4: B_0-maps measured with AMR sensors at 2 K in zero RF field after cooldown with the following conditions: FC with B_a = 7.5 μT (a), FC with B_a = 11 μT (b), SC with B_a = 7.5 μT (c), SC with B_a = 11 μT (d).

FC, after baking the cavity under vacuum on the test stand at 120 °C for 48 h, resulting in a recovery of the Q_0 at high RF fields, up to the quench limit of ~150 mT.

The flux-trapping efficiency and trapped flux sensitivity were measured with the same method used before baking, described above, and the results were η = (52 ± 3)% for SC and η = (18 ± 2)% for FC, which are nearly the same as before baking. The average trapped flux sensitivity from the SC and FC data sets was S = (3.9 ± 0.2) nΩ/μT, ~ 34% lower than prior to baking.

The quench location was found to be on a grain boundary and an example of the overlay between the T-map during quench and the B-map after quench measured by AMR sensors at 2 K and B_p = 140 mT after SC with $B_a \sim 11\,\mu T$ is
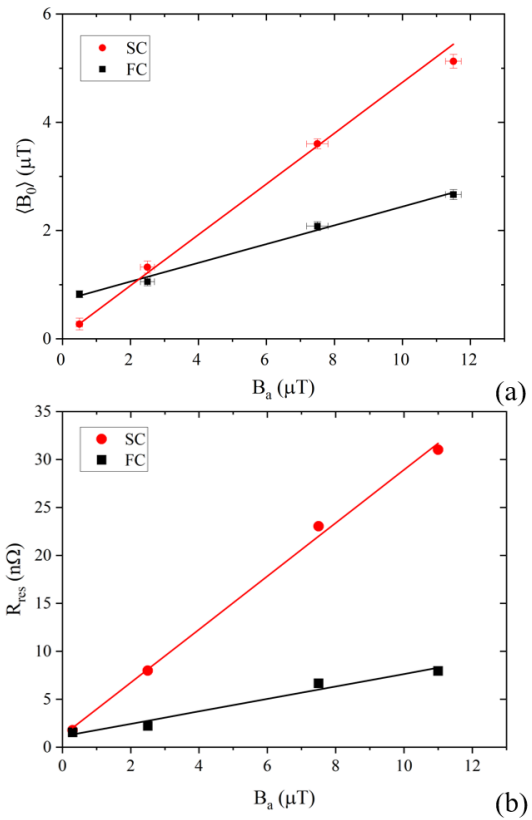

Figure 5: $\langle B_0 \rangle$ measured with AMR sensors at 2 K in zero RF field (a) and R_{res} (b) as a function of the ambient magnetic field during cooldown for FC and SC. The size of the error bars are smaller than the symbols in (b). Solid lines are least-squares fit to the corresponding data.
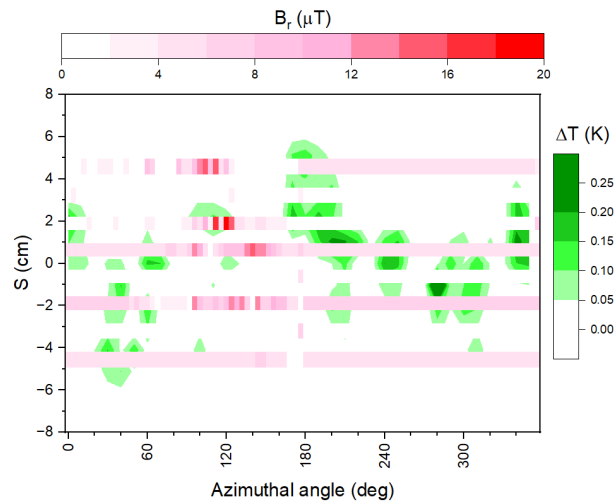

Figure 6: Overlay of unfolded T-map and B-map both measured at 2 K and E_{acc} = 32 MV/m after FC with $B_a \sim 0.5\,\mu T$. The B-map was measured by Hall probes. The variable S is the distance from the equator along the cavity profile. Positive S-values are above the equator. The width of the B-map at the discrete S-positions is not to scale.
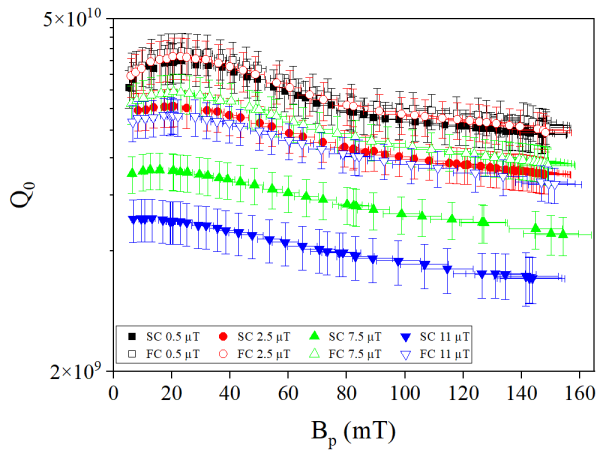
Figure 7: $Q_0(B_p)$ measured at 2 K for different ambient magnetic field and cooldown rate at T_c after baking at 120 °C for 48 h.

Figure 9: ΔT at the quench location measured at 2 K with increasing RF field, prior to quench, and for decreasing RF field after quench.

shown in Fig. 8. A similar B-map was measured by Hall probes. The trapped flux B_0 at $S = -0.6$ cm increased from ~ 0.9 µT before quench to ~ 13.5 µT after quench. The increase in trapped flux at the quench location correlates with an increase in the temperature at the quench location, after quench, resulting in hysteretic $\Delta T(B_p)$, as shown in Fig. 9.

after different cooldown conditions. The increase in trapped flux after quench at the quench location ($S = -0.6$ cm and 120° angle), correlates with a higher magnetic field applied during cooldown, as well as with a SC, for the same B_a, as shown in Fig. 11.
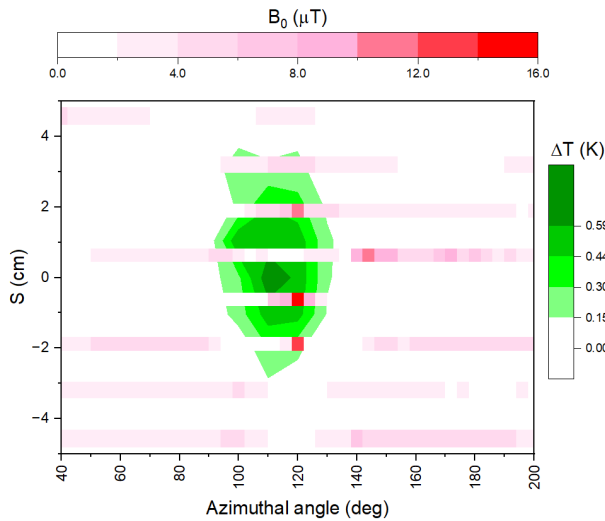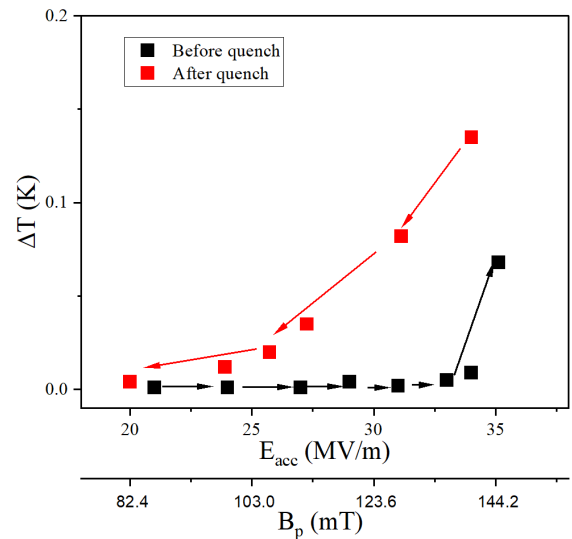

Figure 8: Overlay of unfolded T-map during quench after baking and B-map after quench measured by AMR sensors at 2 K and $B_p = 132$ mT after SC with B_a ~ 11 µT. The variable S is the distance from the equator along the cavity profile. Positive S-values are above the equator. The width of the B-map at the discrete S-positions is not to scale.
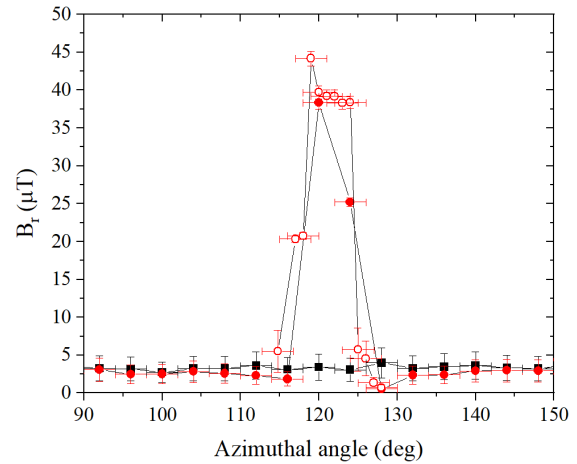

Figure 10: B_r measured by the Hall probe at $S = -0.6$ cm, at 2 K and $B_p = 132$ mT before (squares) and after (solid circles) quench. The empty circles refer to a 13°-wide, fine-resolution scan measured after quench. Solid lines are guides to the eyes.

Figure 10 shows B_r measured by the Hall probe at $S = -0.6$ cm, 2 K, and $B_p = 132$ mT before and after quench and with a smaller angular step after quench. Hall probes have a higher spatial resolution than AMR sensor. The high-trapped flux is distributed over ~ 5° azimuthal angle, corresponding to a width of ~ 1 cm. The same behavior discussed for the case of SC with B_a ~ 11 µT was found

DISCUSSION AND SUMMARY

The availability of a high-resolution magnetic field mapping system allows a better understanding of the flux-trapping phenomenon in SRF cavities and its impact on the RF losses. Some interesting results from the measurements of magnetic and temperature maps of a large-grain
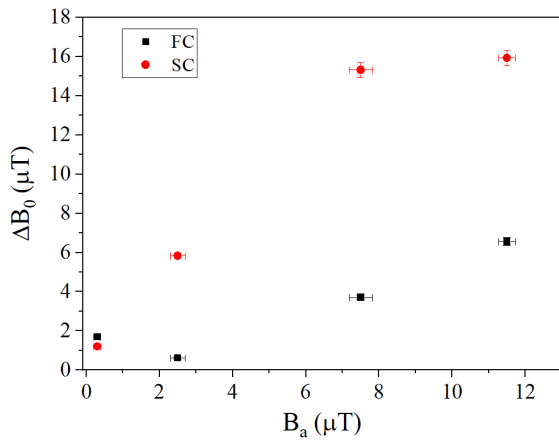
Figure 11: Difference between B_0 at 2 K and $B_p = 132$ mT at the quench location, before and after quench for different values of B_a and for FC and SC. The data were measured by the AMR sensor at $S = -0.6$ cm.

1.3 GHz single-cell cavity, before and after low-temperature baking can be summarized as follows:

- The flux-trapping efficiency was ~ 50% after SC and ~ 20% after FC. While the area covered by the magnetic field sensors is still a small fraction of the total area, it is significantly larger than that measured by a few flux-gate magnetometers at fixed locations, currently used to determine the ability of a cavity to trap magnetic flux.
- The trapped flux sensitivity was ~ 6 nΩ/μT before baking and ~ 4 nΩ/μT after baking, consistently with the values reported in Ref. [13].
- A redistribution of trapped flux was measured at some locations by increasing the RF field from 0 to above 100 mT.
- The extrapolation of the average trapped flux to zero applied magnetic field during FC results in a finite value. This may be related to spontaneous generation of vortices at the SC-NC transition boundary.
- No strong correlation was found between regions of trapped flux and hot-spots causing the high-field Q-slope.
- A redistribution of trapped flux, concentrating at the quench location was found as a result of quenching at 140 mT, similarly to the results in Ref. [26]. The amount of the local trapped flux after quench increases with increasing B_a or with SC, during cool-down below 9.2 K. These results can be explained as follows: the magnetic field that was trapped in the region of the cavity that transitions to the normal-state during quench is released into that region during quench. The area of the normal-conducting region shrinks as the whole cavity returns into the superconducting state, upon reducing the input power. As a result of the normal-area collapsing towards the center, the magnetic field is pushed towards the center, which is the last part of the cavity

to become superconducting, and it is trapped there as vortices. This is shown schematically in Fig. 12.
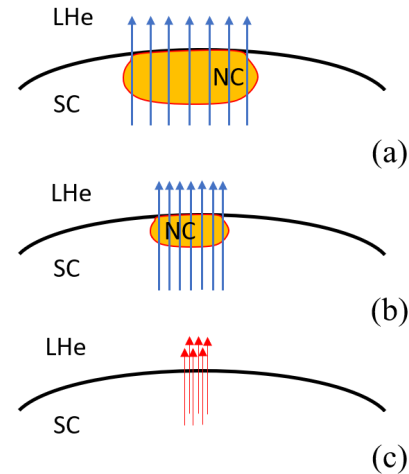

Figure 12: The magnetic field initially trapped in the cavity within the extent of the quench region is confined within the normal-conducting region during quench (a). As the cavity recovers from the quench, the magnetic field is pushed towards the center of the normal-region (b) and it is trapped there as vortices (red lines) as this last region become superconducting (c).

Further studies are planned to investigate the magnitude and location of trapped flux in SRF single-cell cavities made of Nb material with different amount of cold-work and annealing and for bi-metallic cavities.

ACKNOWLEDGMENTS

REFERENCES

[1] H. Padamsee, J. Knobloch, and T. Hays, *RF Superconductivity for Accelerators*, New York, NY:J. Wiley & Sons, 1998.

[2] A. Gurevich and G. Ciovati, "Dynamics of vortex penetration, jumpwise instabilities, and nonlinear surface resistance of type-II superconductors in strong rf fields", *Phys. Rev. B*, vol. 77, p. 104501, Mar. 2008.
    doi:10.1103/PhysRevB.77.104501

[3] S. Aull, O. Kugeler, and J. Knobloch, "Trapped magnetic flux in superconducting niobium samples", *Phys. Rev. Spec. Top. Accel. Beams*, vol. 15, p. 062001, Jun. 2012.
    doi:10.1103/PhysRevSTAB.15.062001

[4] J.-M. Vogt, O. Kugeler, and J. Knobloch, "Impact of cool-down conditions at T_c on the superconducting rf cavity quality factor", *Phys. Rev. Spec. Top. Accel. Beams*, vol. 16, p. 102002, Oct. 2013.
    doi:10.1103/PhysRevSTAB.16.102002

[5] A. Gurevich and G. Ciovati, "Effect of vortex hotspots on the radio-frequency surface resistance of superconductors", *Phys. Rev. B*, vol. 87, p. 054502, 2013. doi:10.1103/PhysRevB.87.054502

[6] A. Romanenko *et al.*, "Ultra-high quality factors in superconducting niobium cavities in ambient magnetic fields up to 190 mG", *Appl. Phys. Lett.*, vol. 105, p. 234103, 2014. doi:10.1063/1.4903808

[7] S. Posen *et al.*, "Efficient expulsion of magnetic flux in superconducting radiofrequency cavities for high Q applications", *J. Appl. Phys.*, vol. 119, p. 213903, 2016. doi:10.1063/1.4953087

[8] T. Kubo, "Flux trapping in superconducting accelerating cavities during cooling down with a spatial temperature gradient", *Prog. Theor. Exp. Phys.*, vol. 2016, p. 053G01, 2016. doi:10.1093/ptep/ptw049

[9] J. Köszegi, O. Kugeler, D. Abou-Ras, J. Knobloch, and R. Schäfer, "A magnetooptical study on magnetic flux expulsion and pinning in high-purity niobium", *J. Appl. Phys.*, vol. 122, p. 173901, Nov. 2017. doi:10.1063/1.4996113

[10] M. Martinello *et al.*, "Magnetic flux studies in horizontally cooled elliptical superconducting cavities", *J. Appl. Phys.*, vol. 118, p. 044505, Jul. 2015. doi:10.1063/1.4927519

[11] S. Huang, T. Kubo, and R. Geng, "Dependence of trapped-flux-induced surface resistance of a large-grain Nb superconducting radio-frequency cavity on spatial temperature gradient during cooldown through T_c", *Phys. Rev. Accel. Beams*, vol. 19, p. 082001, Aug. 2016. doi:10.1103/PhysRevAccelBeams.19.082001

[12] D. B. Liarte *et al.*, "Vortex dynamics and losses due to pinning: Dissipation from trapped magnetic flux in resonant superconducting radio-frequency cavities", *Phys. Rev. Appl.*, vol. 10, p. 054057, Nov. 2018. doi:10.1103/PhysRevApplied.10.054057

[13] P. Dhakal, G. Ciovati, and A. Gurevich, "Flux expulsion in niobium superconducting radio-frequency cavities of different purity and essential contributions to the flux sensitivity", *Phys. Rev. Accel. Beams*, vol. 23, p. 023102, 2020. doi:10.1103/PhysRevAccelBeams.23.023102

[14] F. Kramer, O. Kugeler, J.-M. Köszegi, and J. Knobloch, "Impact of geometry on flux trapping and the related surface resistance in a superconducting cavity", *Phys. Rev. Accel. Beams*, vol. 23, p. 123101, Dec. 2020. doi:10.1103/PhysRevAccelBeams.23.123101

[15] W. Pathirana and A. Gurevich, "Nonlinear dynamics and dissipation of a curvilinear vortex driven by a strong time-dependent Meissner current", *Phys. Rev. B*, vol. 101, p. 064504, Feb. 2020. doi:10.1103/PhysRevB.101.064504

[16] W. P. M. R. Pathirana and A. Gurevich, "Effect of random pinning on nonlinear dynamics and dissipation of a vortex driven by a strong microwave current", *Phys. Rev. B*, vol. 103, p. 184518, May 2021. doi:10.1103/PhysRevB.103.184518

[17] D. Longuevergne and A. Miyazaki, "Impact of geometry on the magnetic flux trapping of superconducting accelerating cavities", *Phys. Rev. Accel. Beams*, vol. 24, p. 083101, Aug. 2021. doi:10.1103/PhysRevAccelBeams.24.083101

[18] S. Balachndran *et al.,* "Direct evidence of microstructure dependence of magnetic flux trapping in niobium", *Sci. Rep.*, vol. 11, p. 5364, 2021. doi:10.1038/s41598-021-84498-x

[19] I. P. Parajuli, G. Ciovati, and J. Delayen, "High resolution diagnostic tools for superconducting radio frequency cavities", *Rev. Sci. Instrum.*, vol. 9, p. 113305, 2022. doi:10.1063/5.0117868

[20] I. P. Parajuli, A. V. Gurevich, G. Ciovati, and J. R. Delayen, "Preliminary Results from Magnetic Field Scanning System for a Single-Cell Niobium Cavity", in *Proc. SRF'21*, East Lansing, MI, USA, Jun.-Jul. 2021, pp. 96. doi:10.18429/JACoW-SRF2021-SUPFDV015

[21] B. Aune *et al.*, "Superconducting TESLA cavities", *Phys. Rev. Spec. Top. Accel. Beams*, vol. 3, p. 092001, 2000. doi:10.1103/PhysRevSTAB.3.092001

[22] I. P. Parajuli, G. Ciovati, and J. R. Delayen, "Magnetic field sensors for detection of trapped flux in superconducting radio frequency cavities", *Rev. Sci. Instrum.*, vol. 92, p. 104705, Oct. 2021. doi:10.1063/5.0063177

[23] G. Ciovati, "Investigation of the superconducting properties of niobium radio-frequency cavities", Ph.D. dissertation, Dept. of Phys., Old Dominion University, Norfolk, VA, 2005.

[24] H. Padamsee, *RF Superconductivity. Science, Technology, and Applications*. Weinheim, Germany:Wiley-VCH, 2009.

[25] G. Ciovati, P. Dhakal, and A. Gurevich, "Decrease of the surface resistance in superconducting niobium resonator cavities by the microwave field", *Appl. Phys. Lett.*, vol. 104, p. 092601, 2014. doi:10.1063/1.4867339

[26] T. Okada *et al.*, "Observation of quenching-induced magnetic flux trapping using a magnetic field and temperature mapping system", *Phys. Rev. Accel. Beams*, vol. 25, p. 082002, 2022. doi:10.1103/PhysRevAccelBeams.25.082002